Disentangling the phase sequence and correlated critical properties in $Bi_{0.7}La_{0.3}FeO_3$ by structural studies

M. M. Gomes,[1] T. T. Carvalho,[1] B. Manjunath,[1] R. Vilarinho,[1] A. S. Gibbs,[2] K. S. Knight,[3,4] J. A. Paixão,[5] V. S. Amaral,[6] A. Almeida,[1] P. B. Tavares,[7] and J. Agostinho Moreira[1,*]

[1]*IFIMUP, Departamento de Física e Astronomia da Faculdade de Ciências, Universidade do Porto, Rua do Campo Alegre s/n, 4169-007 Porto, Portugal*

[2]*HRPD, ISIS Facility, Rutherford Appleton Laboratory, Chilton, Didcot, Oxfordshire OX11 0LA, United Kingdom*

[3]*Department of Materials Science and Engineering, University of Sheffield, Sheffield S1 3JD, United Kingdom*

[4]*Department of Earth Sciences, The Natural History Museum, Cromwell Road, London SW15 5BD, United Kingdom*

[5]*CFisUC, Department of Physics, University of Coimbra, P-3004-516 Coimbra, Portugal*

[6]*CICECO-AIM and Physics Department, University of Aveiro, 3810-193 Aveiro, Portugal*

[7]*Centro de Química-Vila Real, ECVA, Chemistry Department, Universidade de Trás-os-Montes e Alto Douro, 5000-801 Vila Real, Portugal*

(Received 23 September 2021; accepted 2 November 2021; published 18 November 2021)

This work addresses the study of the high-temperature phase sequence of $Bi_{0.7}La_{0.3}FeO_3$ by undertaking temperature-dependent high-resolution neutron powder diffraction (NPD) and Raman spectroscopy measurements. A determination of lattice parameters, phase fractions, and modulation wave vector was performed by Pawley refinement of the NPD data. The analysis revealed that $Bi_{0.7}La_{0.3}FeO_3$ exhibits an incommensurate modulated orthorhombic $Pn2_1a(00\gamma)000$ structure at room temperature, with a weak ferromagnetic behavior, likely arising from a canted antiferromagnetic ordering. Above $T_1 = 543$ K, the low-temperature modulated $Pn2_1a(00\gamma)000$ evolves monotonically into a fractionally growing *Pnma* structure up to $T_N = 663$ K. At 663 K, the low-temperature canted antiferromagnetic phase is suppressed concurrently with the switching of the former into a nonmodulated $Pn2_1a$ structure that continues to coexist with the *Pnma* one, until the latter is expected to reach the 100% fraction of the sample volume at high temperatures above 733 K. The $Pn2_1a$ space group is obtained from the *Pnma* one through the Γ_4^- polar distortion. Neutron diffraction and Raman spectroscopy results provide evidence for the emergence of noteworthy linear spin-phonon coupling. In this regard, magnetostructural coupling is observed below T_N, revealed by the relation between the weak ferromagnetism of the canted iron spins and the FeO_6 octahedra symmetric stretching mode. The correlation between magnetization and structural results from NPD provides definite evidence for the magnetic origin of the structural modulation. The analysis of the temperature-dependent magnetization and the magnetic peak intensity as well yields a critical exponent (β) value of 0.38. The lower limit of the phase coexistence temperature $T_1 = 543$ K, marking the emergence of the *Pnma* phase, is also associated with the temperature whereupon the modulation magnitude starts to decrease.

DOI: 10.1103/PhysRevB.104.174109

I. INTRODUCTION

Multiferroic materials have received intensive widespread consideration in recent years because of their manifold promising technological applications in multiple-state memories, sensors, actuators, transducers and electric-field ferromagnetic resonance controllers [1,2].

Bismuth ferrite (BFO) has been extensively investigated as one of the most representative multiferroics, bearing both magnetic and ferroelectric orders at ambient conditions, associated with noticeably high Néel ($T_N \sim 630$ K) and Curie ($T_C \sim 1100$ K) temperatures [3]. BFO exhibits, at room temperature, a rhombohedral distorted perovskite structure with $R3c$ symmetry, associated with Bi^{3+} ion displacements along the $[111]_{pc}$ direction, and oxygen octahedra antiferrodistortive counter-rotations about the same axis [4,5]. The ferroelectric polarization emerges from the large displacement of the Bi^{3+} ions associated with their stereoactive $6s^2$ lone pair of electrons, while the magnetization follows from the superexchange interaction between the high-spin configured Fe^{3+} ions [3,5]. Though the superexchange rules yield a G-type antiferromagnetic arrangement, a canted magnetic moment emerges due to Dzyaloshinskii-Moriya interactions. Moreover, a long-range incommensurate spin cycloidal with a period of ~ 620 Å is additionally induced through an inhomogeneous magnetoelectric mechanism [6–8].

Despite these promising characteristics, a plethora of problems jeopardize the capability to develop BFO-based devices. Some of them include low remnant polarization, high leakage currents, secondary phases, and weak magnetization contributing to the weakening of the magnetoelectric coupling [3,6]. Different attempts have been made in order to overcome these limitations, such as different processing techniques [9,10] or partial substitution of the Bi-site using rare-earth ions, such as La^{3+} or Pr^{3+}, and/or the Fe-site with

*Corresponding author: jamoreir@fc.up.pt

 ©2021 American Physical Society

transition-metal ions [11–16]. It has been considered that the isovalent substitution of bismuth by rare-earth elements can prevent the emergence of secondary phases and destabilize the incommensurate spin cycloid by improving magnetocrystalline anisotropy, hence yielding more favorable conditions improving multiferroicity [17]. Since rare-earth orthoferrites crystallize at ambient conditions in a nonpolar *Pnma* symmetry, and $BiFeO_3$ exhibits polar $R3c$ symmetry, the disorder induced through partial rare-earth substitution should lead to a decoherence of the Bi^{3+} stereoactive $6s^2$ electron lone pairs, and consequently yield a symmetry change from the polar to the nonpolar space group [18–24].

Yet, the way pursued between those types of symmetries depends significantly on the substituting rare-earth ion, and a large debate persists regarding the actual phase transition sequence and correlated critical properties, in particular the magnetic and polar properties [2].

A significant number of studies have been focused on the $Bi_{1-x}La_xFeO_3$ solid solution using different processing methods and conditions of sample synthesis. It was generally demonstrated that the choice of the synthesis route and temperature is a key issue, as it has a huge effect on its properties and can hinder the processing of single-phase ceramics.

Room-temperature computational and experimental investigations point out that for low La^{3+} concentration ($x < 0.2$), an $R3c$ symmetry is assumed [12,19,25–29]. Though quite different phases have been previously suggested for $x \geqslant 0.2$, it is now commonly assumed that an orthorhombic symmetry is stabilized. For $0.20 \leqslant x \leqslant 0.45$, an incommensurate modulated (IM) orthorhombic phase is formed, wherein two different types of superspace groups have been reported, namely $Imma(00\gamma)s00$ [22] and $Pn2_1a(00\gamma)s00$ [12,20,24]. The latter superspace group was chosen by Carvalho *et al.* [20], since, on the one hand, it presents relative to the other one lower *R*-factors stemming from a more precise refinement of the satellite peaks, and on the other hand it is compatible with the ferroelectric and piezoelectric behavior ascertained in that composition range. Though the modulation has been indexed through two different types of superspace groups, it can be noticed that the proposed underlying mechanisms for the emergence of the incommensurate modulated orthorhombic phase are almost identical, consisting in the polar displacement of Bi and O(1) ions toward each other along the crystallographic *a* axis, and by the displacement of the O(2) ions within the *ab* plane. It is thus likely that the driving force for the emergence of incommensurability arises from the coupling between the polar displacements and the symmetric stretching mode through the lattice strain. This interpretation requires further confirmation, since the uncertainty associated with the determination of the atomic positions still hinders a full understanding of its complex nature. For the concentration region $x > 0.45$, it has been generally accepted that a single $LaFeO_3$-type *Pnma* phase is stabilized, which can be corroborated by the work of Kavanagh *et al.*, wherein a comprehensive neutron diffraction study on $Bi_{0.5}La_{0.5}FeO_3$ is reported [19,30,31].

Contrary to room-temperature studies, few works have been devoted to untangling the phase-transition sequence of the $Bi_{1-x}La_xFeO_3$ solid solution and the corresponding critical behavior [2,15,18,22,24,31–33]. Though some partial contradictory results were reported, the phase diagram reported by Perejón *et al.* can be understood as a good representative example of its general profile [24]. A phase line associated with the structural phase transition to the *Pnma* phase can be observed up to $x \sim 0.30$, which steeply decreases with a slope of ~17 K/%La. Another phase line is also apparent, which represents the antiferromagnetic-paramagnetic phase transition and slightly increases with a slope of ~ 1 K/%La. It is worth stressing that the two phase lines cross in the vicinity of the 30% La concentration, which suggests a special role of this La concentration in the phase diagram. Moreover, a phase coexistence region centered at $x \sim 0.15$ is observed, involving the transition from the rhombohedral to the modulated orthorhombic structure [12]. One of the most relevant outcomes is the stabilization of an incommensurate modulated orthorhombic structure for $0.15 < x \leqslant 0.30$, whose upper temperature limit is still an intriguing issue and deserves further attention. Moreover, if we also take into consideration the phase coexistence ascertained by Rusakov *et al.* for $x = 0.25$, ranging from about 670 to 870 K, these issues anticipate a much more complex scenario regarding the profile of the phase diagram at least in this range of concentrations [22]. Consequently, such a scenario must have a strong impact on the structural properties leading to a specific phase transition sequence and corresponding critical behavior. Such phenomena may involve the coupling between lattice and spin degrees of freedom, and also between polar displacement and the symmetric stretching mode, which in turn will determine the behavior of ferroelectric and magnetic properties throughout the phase transitions. These key issues have to be embraced to reach a comprehensive correlation between structure, magnetism, and ferroelectricity.

To address these questions, we have selected the $Bi_{0.7}La_{0.3}FeO_3$ solid solution, as it is located at the upper frontier of a privileged region of the (%La,T) phase diagram, and both the phase transition sequence and the critical physical behavior are still very poorly understood. $Bi_{0.7}La_{0.3}FeO_3$ will be structurally studied through high-resolution neutron powder diffraction and Raman spectroscopic techniques from room temperature up to ~750 K. The set of data will be analyzed by comprehensible models, and, expectedly, the obtained results will enable us to elucidate phase coexistence and symmetry, the temperature dependence of the lattice parameters and wave modulation, as well as the structural distortions and magnetic parameters associated with the ferroelectric and magnetic phase transitions, respectively. Finally, a discussion highlighting the most definite physical outcomes will be presented.

II. EXPERIMENTAL DETAILS

A $Bi_{0.7}La_{0.3}FeO_3$ sample was prepared by the sol-gel combustion method as reported elsewhere [20]. The resulting powders were calcinated at 550 °C, reground, pelletized, and thermally treated at 870 °C for 3 h.

Neutron powder diffraction data for $Bi_{0.7}La_{0.3}FeO_3$ composition were collected at the ISIS Pulsed Neutron and Muon Facility of the Rutherford Appleton Laboratory (UK) on the high-resolution powder diffractometer (HRPD). The sample was sealed in a thin-walled vanadium can, which was then

mounted in a standard RAL furnace. Data were taken at different fixed temperatures from 303 to 733 K. Appropriate equilibrium times were included upon each change of temperature. The data were collected simultaneously using three different detector banks: backscattering, 90º, and low angle bank, with d-spacing ranges ∼0.6–2.6, ∼0.9–3.9, and ∼2.3−10.2 Å, respectively. Pawley refinements of the crystal structures were performed using GSAS-II software [34].

Raman spectra were recorded using a Renishaw inVia Qontor spectrometer with a 532 nm linearly polarized diode-pumped laser, in the spectral range 100–800 cm^{-1}. Bragg filters were also used allowing a spectral range of −250 to 250 cm^{-1}. Measurements were done at fixed temperatures from 294 to 733 K using a THMS600 Linkam Stage. The effect of the laser power on the sample was previously studied to prevent the heating of the sample. The wave-number temperature dependence of the Raman modes was determined by the best fit of a sum of damped oscillators to the experimental spectra, according to the general formula [35]

$$I(\omega, T) = (1 + n(\omega, T)) \sum_{j=1}^{N} A_{0j} \frac{\omega \Omega_{0j}^2 \Gamma_{0j}}{\left(\Omega_{0j}^2 - \omega^2\right)^2 + \omega^2 \Gamma_{0j}^2}, \quad (1)$$

where $n(\omega, T)$ is the Bose-Einstein temperature factor, and A_{0j}, Ω_{0j}, and Γ_{0j} are the amplitude, the frequency, and the damping factor for the jth normal mode. The fitting was made with the software package IGORPRO (WAVEMETRICS®).

Temperature-dependent magnetic measurements, $M(T)$, were performed in an Oxford Instrument VSM, equipped with a furnace, and the measurements were made at a constant magnetic field of 0.1 T.

III. RESULTS

A. High-resolution neutron powder diffraction

Representative NPD patterns recorded at different fixed temperatures, in the d-spacing range of the backscattering bank, from 0.75 to 2.50 Å, and the low angle bank, from 3.50 to 6.25 Å, are shown in Figs. 1(a) and 1(b), respectively. The chosen temperatures for which NPD patterns are shown were selected to highlight significant changes in the diffraction profiles, apparent in the 1.72–1.80 Å d-spacing ranges that are much better resolved in Fig. 1(c).

It is evident that the diffraction patterns at 563 K show peaks that are not observed at 543 K. This feature suggests that structural changes occur in between those temperatures. Moreover, the intensity of some peaks decreases upon heating, and simultaneously some new diffraction peaks [marked with arrows in Fig. 1(c)] emerge, whose intensity increases upon further heating above 563 K. For example, Fig. 1(c) shows representative peaks of $Bi_{0.7}La_{0.3}FeO_3$ at 1.755 and 1.77 Å (room-temperature values), whose intensity decreases above 563 K. The emergence of new reflections above 563 K, and their coexistence with the reflections already observed from the room-temperature structural phase up to 733 K, is a noteworthy indication for phase coexistence phenomena observed in a temperature range from 563 to 733 K (spanning over more than 170 K). This rather larger temperature range is apparently a quite uncommon outcome.

The intensity of the peak at ∼4.54 Å [see Fig. 1(b)] monotonically decreases as temperature increases from 303 K and eventually disappears above T_N. This peak has been ascribed to a magnetic diffraction, corresponding to the (101/003) reflections observed by Sosnowska *et al.* for $BiFeO_3$ [7,8]. Furthermore, the small peak observed close to 4.90 Å has been assigned to a structural satellite peak of the $Pn2_1a(00\gamma)s00$ superspace group. It is worth noting that this peak does not exist above T_N.

In our previous work, we reported the superspace group $Pn2_1a(00\gamma)s00$ instead of $Pn2_1a(00\gamma)000$ for $Bi_{0.7}La_{0.3}FeO_3$ based on room-temperature XRD studies [12,20] due to the existence of a peak at 3.30 Å that was assigned to a satellite reflection. However, our temperature-dependent NPD data revealed that this peak remains up to the highest measured temperature (733 K), indicating that it cannot be a satellite peak, as it should vanish above T_N [see Fig. 1(d)]. Consequently, in this work, the $Pn2_1a(00\gamma)000$ superspace group will be used, which predicts all the satellite peaks of the former one, except the peak at ∼3.30 Å.

The 303–733 K temperature range can be divided into three specific stability phase regions. The first one is a single-phase region that spans from room temperature to T_1, a temperature somewhere between 543 and 563 K to be carefully defined in the following. Considering that the room-temperature crystal symmetry is described by the $Pn2_1a(00\gamma)000$ superspace group [12,20], by continuity, the crystal structure in the 300 K − T_1 range has this symmetry, overall. The second one, ranging from T_1 to 733 K, corresponds to a phase coexistence region. Though we are not considering subtle key symmetry features, in general this region can be characterized by the coexistence of two different crystallographic structures and magnetic ordering.

To fully characterize the changes observed through visual evaluation of the NPD patterns from Fig. 1, a detailed Pawley refinement analysis was performed for all the data collected at different fixed temperatures. In this work, only the crystallographic structural refinement was carried out. A systematic magnetic structure analysis, as has been performed with HRPD data [36], was not viable with the current data due to the use of a 30–130 ms time-of-flight range in the interests of high-quality structural investigations [37,38].

Figures 2(a)–2(c) show Pawley refinements done on the NPD patterns recorded at temperatures of 303, 613, and 733 K, respectively, corresponding to the representative examples for each of the aforementioned stability temperature regions. For the sake of clarity, the refinement result of the most intense reflections at 303, 613, and 733 K is shown in Fig. 3.

Pawley analysis of all the NPD patterns reveals that up to 543 K (see Fig. S1 of the Supplemental Material [39]), except for the weak peak at 1.97 Å [better seen in Fig. 3(a)], all the observed diffraction peaks are indexed by using the $Pn2_1a(00\gamma)000$ superspace group, confirming the single-phase nature of the aforementioned first phase region. The intensity of the nonindexed peak, observed at 1.97 Å, changes slightly with temperature up to 543 K. Above this temperature its intensity increases, and the peak is well indexed to the *Pnma* phase [see Figs. 3(b) and 3(c)]. Below 543 K, we interpret this peak as a spurious reflection emerging from

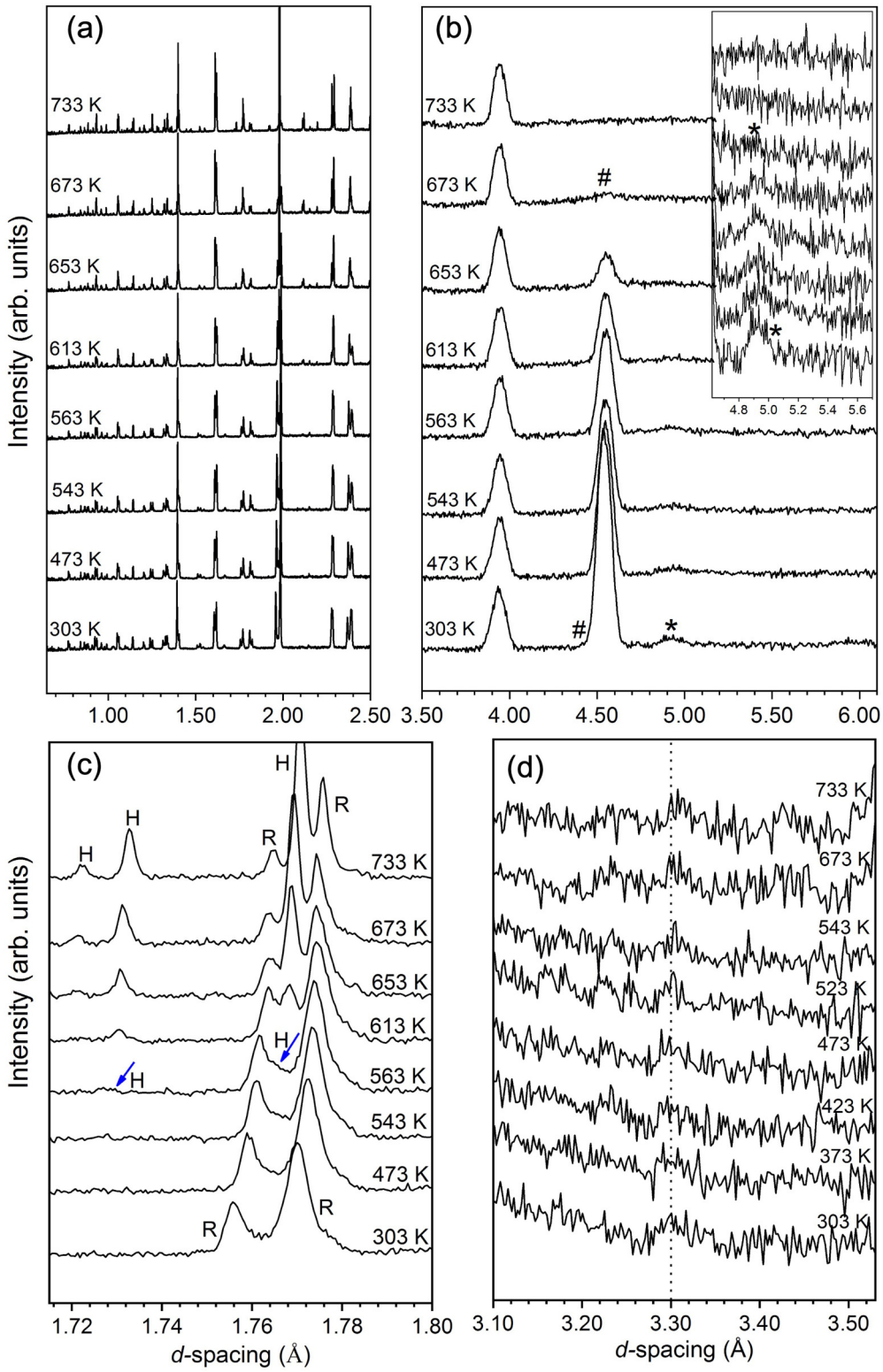

FIG. 1. Representative neutron diffraction patterns recorded at different fixed temperatures obtained through HRPD in the d-spacing regions (a) 0.75–2.50 Å and (b) 3.50–6.25 Å, regarding the backscattering and low angle banks, respectively. # and * correspond to the magnetic peak at 4.54 Å and the satellite peak at 4.90 Å, respectively. The inset shows the magnified region of the low angle bank for the same order of temperature as given in (b), evidencing the satellite peak. (c) Magnified region ranging from 1.716 to 1.80 Å d-spacing, to highlight the coexistence of peaks coming from R, room-temperature phase; and from H, high-temperature phase. (d) d-spacing region 3.10–3.50 Å from 90º bank, showing the spurious peak at ∼3.30 Å that remains up to the highest temperature.

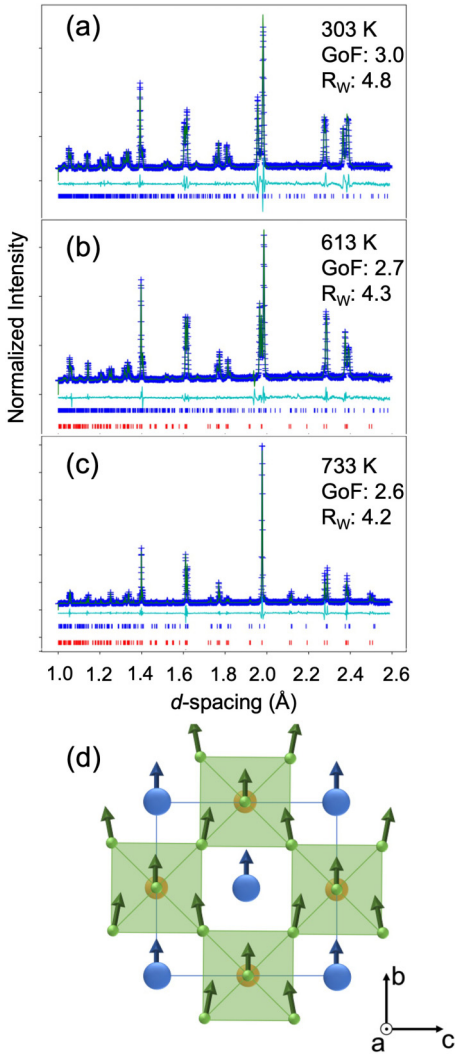

FIG. 2. Pawley refinements of NPD patterns obtained from the backscattering bank at (a) 303 K, (b) 613 K, and (c) 733 K, using $Pn2_1a(00\gamma)000$ (blue), $Pn2_1a(00\gamma)000$ (blue) + *Pnma* (red), and $Pn2_1a$ (blue) + *Pnma* (red) symmetries, respectively. (d) Schematic *a*-axis view of the Γ_4^- polar distortion (Bi in blue, Fe in orange, and O in green).

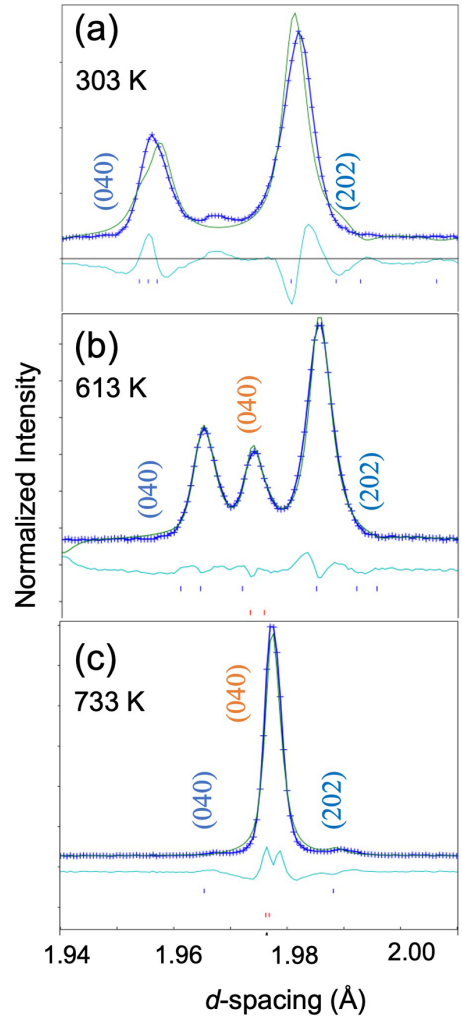

FIG. 3. Magnified images of the Pawley refinements of NPD obtained in HRPD for (a) 303 K, (b) 613 K, and (c) 733 K: The panels show the most intense reflections from the $Pn2_1a(00\gamma)000$ phase. Blue color reflections are from the $Pn2_1a(00\gamma)000$ and $Pn2_1a$ phases, and red ones are from the *Pnma* phase.

a very small percentage of *Pnma* phase (less than 1%), or from compounds used to manufacture the furnace, wherein the sample was mounted [35].

All the patterns comprised in the second phase region, $T_1 < T < T_N$, are well described using a $Pn2_1a(00\gamma)000$ + *Pnma* model, confirming the distinct type of phase coexistence referred to above. It is worth noting that for the *Pnma* phase, the initial refinement parameters were taken from Rusakov *et al.* [22]. In the $T_N < T < 733$ K range, all the encompassed diffraction peaks can be very well indexed using the Pawley refinement method, wherein a coexistence of $Pn2_1a$ and *Pnma* phases is assumed. This result fully confirms the aforementioned assumption regarding the coexistent nature of the second phase region between T_N and 733 K.

To unravel the kind of atomic distortion correlation that occurs between the $Pn2_1a$ and the prototype *Pnma* space group, we have further performed a symmetry-adapted mode analysis. According to the Amplimodes tool of the Bilbao Crystallographic Server, the $Pn2_1a$ is obtained from the *Pnma* symmetry through the Γ_4^- polar distortion, which involves the displacements of the Bi^{3+} and O^{2-} ions with regard to their positions in the high-temperature phase, while the Fe^{3+} cations keep the same position, as depicted in Fig. 2(d), giving rise to the electric polarization along the *b*-axis [40].

A specific feature occurs above T_N, which consists of the simultaneous vanishing of both magnetic and structural satellite diffraction peak intensities. It is worth stressing that all observed satellite peaks are indexed using the $Pn2_1a(00\gamma)000$ superspace group, and no other peaks from the magnetic structure could be detected. This result enables us to assign these peaks to the crystallographic modulation. The absence of both magnetic and satellite peaks above T_N is clear evidence of the paramagnetic state of this material, on the one hand, and the disappearance of the structural modulation, on the other hand. This means that the crystallographic structure of $Bi_{0.7}La_{0.3}FeO_3$ is no longer modulated above T_N. This

TABLE I. Linear thermal expansion coefficients determined for different temperature intervals.

Phase symmetry	Temperature range (K)	$\alpha_a \times 10^{-6}(\mathrm{K}^{-1})$	$\alpha_b \times 10^{-6}(\mathrm{K}^{-1})$	$\alpha_c \times 10^{-6}(\mathrm{K}^{-1})$
$Pn2_1a(00\gamma)000$	303 K$-T_1$	8.9 ± 0.8	14.4 ± 0.9	9.6 ± 0.5
$Pn2_1a(00\gamma)000$	T_1-T_N	8.9 ± 0.8	0.16 ± 0.07	9.6 ± 0.5
$Pn2_1a$	T_N-733 K	8.9 ± 0.8	–	9.6 ± 0.5
Pnma	T_N-733 K	8 ± 1	9 ± 2	5.2 ± 0.9

outcome is, as will be discussed below, of key importance regarding the phase sequence and correlated critical properties of $Bi_{0.7}La_{0.3}FeO_3$.

The temperature dependence of the pseudocubic lattice parameters and volume, the modulation wave vector q_3, and the phase fractions throughout the different phase regions is shown in Figs. 4(a)–4(e), respectively, in the whole explored temperature range. The $a_{pc}(T)$ and $c_{pc}(T)$ pseudocubic lattice parameters of both $Pn2_1a(00\gamma)000$ and $Pn2_1a$ phases expand almost linearly as temperature increases in the 303–733 K range, following the same temperature dependence with no hint of changes at $T_1 \sim 543$ K, above which the *Pnma* phase emerges, nor at T_N, above which the satellite peaks are no longer observed. The $b_{pc}(T)$ expands linearly as temperature increases from 303 K to T_1, where the single $Pn2_1a(00\gamma)000$ phase is observed, and above T_1 it becomes temperature-independent up to 733 K. Concerning the *Pnma* phase, all pseudocubic lattice parameters increase linearly with temperature in the T_1-733 K range. Table I shows the direction-dependent linear thermal expansion coefficient determined for different temperature intervals. The a_{pc} and c_{pc} of both $Pn2_1a(00\gamma)000$ and $Pn2_1a$ phases exhibit similar linear thermal expansion coefficients, about 36% smaller than the corresponding value along the *b*-direction in the 303–543 K temperature range. In the *Pnma* phase, different thermal expansion behavior is observed. In fact, both a_{pc} and b_{pc} scale in the same way with temperature, with linear thermal expansion coefficients 36% larger than in the *c*-direction.

Although different temperature behaviors are ascertained regarding the pseudocubic lattice parameters, an effective volume expansion of the corresponding primitive cells is observed in the whole temperature range explored. Interestingly, there is a 0.5% contraction of the primitive cell volume of the *Pnma* phase compared with that of both $Pn2_1a(00\gamma)000$ and $Pn2_1a$ phases, respectively, keeping constant the number of molecules per primitive cell ($Z = 4$). The contraction of the primitive cell stems from the decrease in a_{pc} and c_{pc} parameters, while moving from the $Pn2_1a(00\gamma)000$ or $Pn2_1a$ to the *Pnma* primitive cell. No clear anomalous temperature behavior of the lattice parameters is ascertained at T_N.

Figure 4(d) shows the modulation wave vector q_3 as a function of temperature. q_3 is almost temperature-independent in the 303–543 K range, with $q_3 = 0.476 \pm 0.001$. Above 543 K, $q_3(T)$ decreases monotonously, eventually vanishing at T_N. For comparison purposes, Fig. 4(d) also shows the temperature dependence of the modulation wave vector of $Bi_{0.75}La_{0.25}FeO_3$, reported by Rusakov *et al.* [22]. The q_3 value obtained in this work is about 2% smaller than that reported for the $Bi_{0.75}La_{0.25}FeO_3$ compound. The observed decrease of the modulation wave vector with increasing La content is in good agreement with reported results obtained from XRD studies [12,22]. It is worth stressing that both q_3 modulation vectors vanish practically at similar temperatures (close to T_N), in good agreement with the very small slope of the paramagnetic-antiferromagnetic phase line of the (x,T) phase diagram.

The phase fractions of each crystallographic phase as a function of temperature, obtained from the Pawley refinements [41], are presented in Fig. 4(e). Above 543 K and up to 733 K, the *Pnma* phase emerges and its fraction gradually increases, whereas the $Pn2_1a00\gamma(000)$ phase fraction decreases accordingly. At T_N, wherein the modulation vanishes, 35% of the $Pn2_1a$ phase and 65% of the *Pnma* phase coexist. At the highest studied temperature, 733 K, the *Pnma* and $Pn2_1a$ phases reach a fraction of 90% and 10%, respectively. $Bi_{0.7}La_{0.3}FeO_3$ should eventually attain a single phase *Pnma* symmetry at a higher temperature estimated to be close to 745 K. From the overall results shown in Fig. 4, the magnitude of the aforementioned temperature T_1 can then be assigned a value of ~550 K.

B. Temperature-dependent Raman scattering

Representative unpolarized Raman spectra of $Bi_{0.7}La_{0.3}FeO_3$ recorded at different fixed temperatures, in the −250 to 800 cm^{-1} spectral range, are presented in Figs. 5(a) and 5(b). The spectral profile at room temperature agrees very well with the already published data, which evidence the orthorhombic symmetry of $Bi_{0.7}La_{0.3}FeO_3$ [19]. A broad low-frequency scattered signal is observed, whose intensity increases as temperature increases in such a way that it prevents the observation of the Raman bands located below 50 cm^{-1}. A similar low-frequency tail was reported for $Bi_{1-x}La_xFeO_3$, with $0.15 \leqslant x \leqslant 0.5$, whose intensity increases with increasing x up to 0.5 [19]. This quasielastic scattering signal has been assigned to the disorder arising from the random distribution of the La/Bi cations at the *A*-site [19]. To unravel the origin of this low-frequency signal, we have compared it with the one observed in the Raman spectrum of undoped $BiFeO_3$, recorded in the same spectral range at room temperature and at 653 K, shown in Fig. S2 of the Supplemental Material [39]. It is apparent that in $BiFeO_3$, the quasielastic signal is weaker than in the mixed system in the whole temperature range, confirming the disorder origin of the low-frequency scattered signal in $Bi_{1-x}La_xFeO_3$. We have analyzed the temperature dependence of this tail, but no hints of anomalous temperature behavior could be ascertained in the 294–733 K temperature range.

The lowest wave-number excitation observed in the Raman spectrum of $Bi_{0.7}La_{0.3}FeO_3$ at room temperature is located at 30 cm^{-1}. As temperature increases toward 425 K, due to the

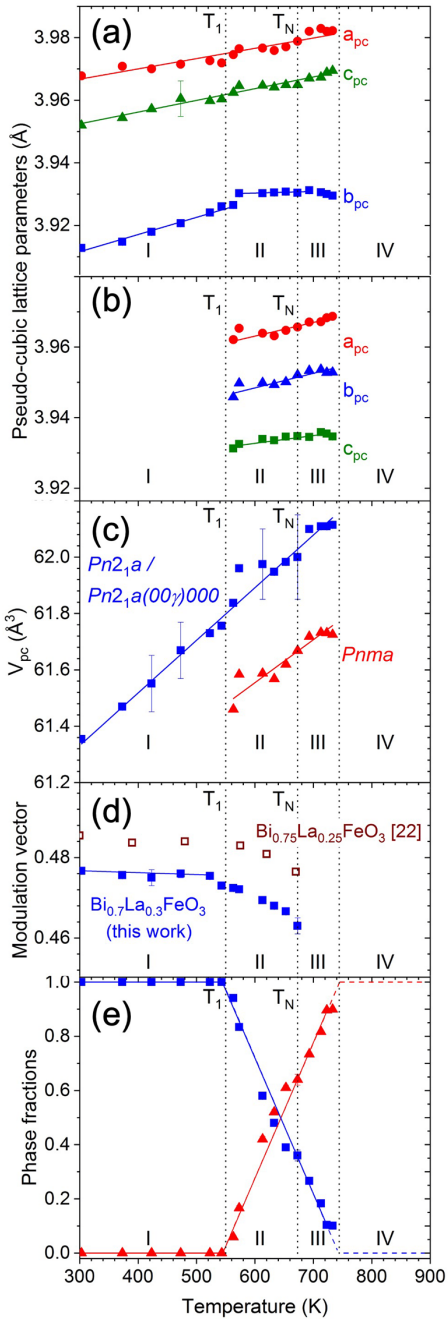

FIG. 4. Temperature dependence of pseudocubic lattice parameters ($a_{pc} = \frac{a}{\sqrt{2}}, b_{pc} = \frac{b}{2}, c_{pc} = \frac{c}{\sqrt{2}}$) for (a) $Pn2_1a$ and $Pn2_1a(00\gamma)000$ phases and for (b) *Pnma* phase; (c) pseudocubic volume for both $Pn2_1a$ and $Pn2_1a(00\gamma)000$ phases (blue symbols) and *Pnma* phase (red symbols); (d) modulation wave vector for $Bi_{0.7}La_{0.3}FeO_3$ and $Bi_{0.75}La_{0.25}FeO_3$ [22]; and (e) phase fractions, obtained by Pawley refinements, wherein the solid lines are guides to the eye, and the horizontal dashed lines are an extrapolation of the expected phase fractions for $T > 733$ K. I: $Pn2_1a(00\gamma)000$; II: $Pn2_1a(00\gamma)000 + Pnma$; III: $Pn2_1a + Pnma$; IV: *Pnma*.

increase of the intensity of the quasielastic scattering signal, the band becomes less resolved and is no longer observed for temperatures higher than 425 K. Nevertheless, while this band is observed in the 294–425 K range, its wave number

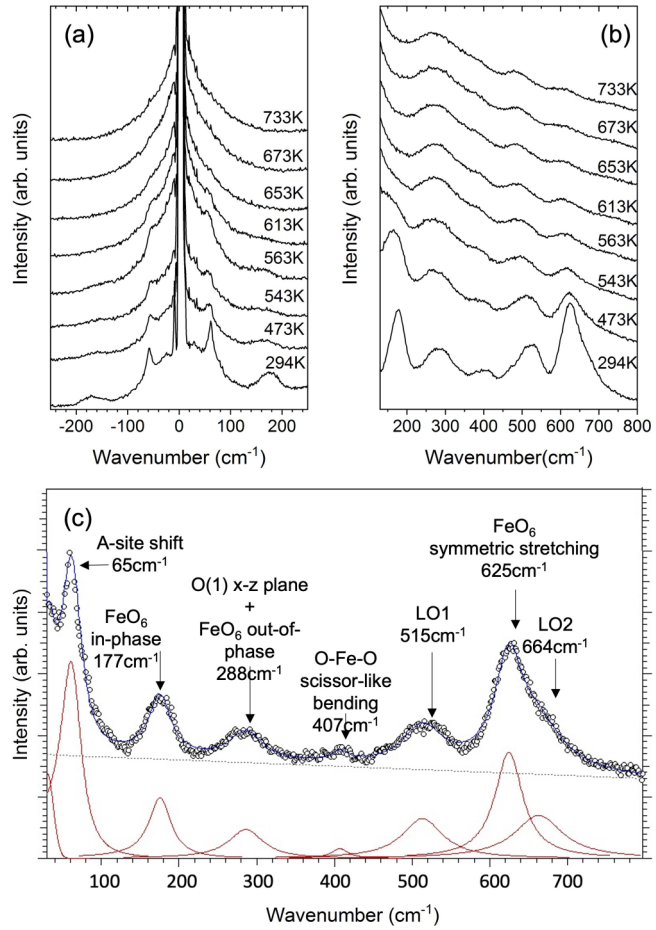

FIG. 5. Raman spectra of $Bi_{0.7}La_{0.3}FeO_3$ recorded at different fixed temperatures in the ranges (a) -250 to 250 cm^{-1} and (b) 100–800 cm^{-1}. (c) Representative example of the best fit of Eq. (1) to the Raman spectrum recorded at room temperature in the 50–800 cm^{-1} spectral range, with seven damped oscillators.

remains almost temperature-independent. The Raman spectrum of $BiFeO_3$ single crystal, recorded at room temperature, exhibits several low-lying excitations below 60 cm^{-1} assigned to magnons [42,43], the so called ϕ_n (spin excitations in the cycloidal plane) and ψ_n (spin excitations out of the cycloidal plane) magnon modes observed in parallel and crossed polarizations, respectively [42]. Contrary to this case, orthorhombic rare-earth ferrites such as the parent compound $LaFeO_3$ exhibit only two Raman-active magnons below 60 cm^{-1} arising from the doubly degenerate magnon branch, whose degeneracy is lifted by the Dzyaloshinskii-Moriya interaction [44,45]. Considering the rather simple magnon spectrum observed at room-temperature conditions, we tentatively assign the band at 30 cm^{-1} to the magnon excitation in $Bi_{0.7}La_{0.3}FeO_3$.

Figure 5(c) shows a representative example of the fit of Eq. (1) to the unpolarized Raman spectrum, recorded at room temperature in the 40–800 cm^{-1} range. We have resolved the Raman spectrum into seven bands in this spectral range [19]. The mode assignment of the observed bands is proposed based on the reliable literature in similar structural compounds [19,20,46], and the corresponding mode assignment is presented in Fig. 5(c). According to Bielecki *et al.* [19], the

forbidden longitudinal optical modes are activated due to the Fröhlich mechanism.

As temperature increases, the bands become broader and overlap, as expected. However, the similar spectra profile observed up to 733 K points out that the orthorhombic structure is kept in the whole explored temperature range. The stabilization of the *Pnma* phase above 543 K, the occurrence of the magnetic phase transition, and the loss of the structural modulation at T_N are not clearly mirrored by significant changes of the Raman signal. Although they are barely noticeable in a qualitative analysis, a quantitative analysis of the spectra reveals anomalous temperature behavior in some Raman modes, associated with structural and magnetic changes occurring at the respective temperatures, as will be addressed in the following section.

IV. DISCUSSION

A. Magnetic origin of the structural modulation

Figure 6(a) shows the nonlinear contribution to the magnetization, $\Delta M(T)$, of $Bi_{0.7}La_{0.3}FeO_3$ as a function of the reduced temperature T/T_N. $\Delta M(T)$ was determined from the subtraction of the mean magnetization value $M_0 = 0.07223$ emu/g, above T_N, from the measured magnetization in ZFC conditions [the experimental $M(T)$ curve is shown in Fig. S3 of the Supplemental Material [39]]. As temperature increases, $\Delta M(T)$ continuously decreases and vanishes at $T_N = 663$ K, marking the transition into the high-temperature paramagnetic phase. The continuous temperature dependence of $\Delta M(T)$ just below T_N points out a second-order nature of the magnetic phase transition, and the nonvanishing magnetization for $T < T_N$ is evidence of the ferromagnetic-like response in this compound, likely due to the spin canting, already evidenced by the $M(H)$ hysteresis loops at room temperature [20].

According to the theory of equilibrium critical phenomena [47,48], in a magnetic system undergoing a second-order phase transition, the critical behavior of the spontaneous magnetization close to the transition temperature (T_N) is given by

$$\Delta M(T) \propto (T_N - T)^{\beta}, \tag{2}$$

where β is the critical exponent. The continuous line in Fig. 6(a) was calculated from the best fit of Eq. (2) to the experimental values in the 530 K-T_N range. The temperature dependence of the magnetization is well described by Eq. (2) with a critical exponent $\beta = 0.384 \pm 0.003$. Below 530 K, the $\Delta M(T)$ data are no longer described by Eq. (2) with a single β exponent.

The magnetic phase transition in $Bi_{0.7}La_{0.3}FeO_3$ is clearly signalized by structural changes, mirrored by the vanishing of several diffraction peaks above T_N. This finding yields clear evidence for the existence of an intrinsic relationship between the stabilization of the magnetic order parameter below T_N and the emergence of the structural modulation. To shed light on the interplay between both magnetic and crystallographic structures, we have analyzed the correlation between the intensities of the diffraction peaks vanishing above T_N and the magnetic order parameter, which is well represented by the nonlinear contribution to the magnetization, $\Delta M(T)$. As an example, we have considered the satellite peak located at 4.90 Å. Figure 6(b) shows the intensity of this peak as a function of T/T_N.

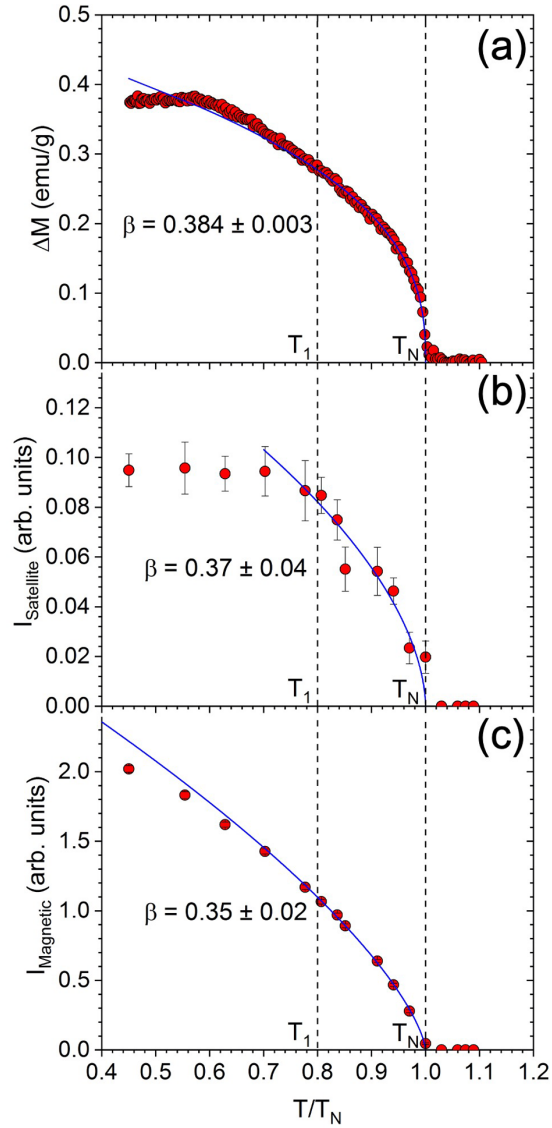

FIG. 6. (a) Reduced temperature dependence of the nonlinear contribution to the magnetization, $\Delta M(T)$. The solid line was calculated from the best fit of Eq. (2) to the experimental results in the 530 K-T_N range. (b) Reduced temperature dependence of the intensity of the satellite peak located at 4.90 Å. (c) Reduced temperature dependence of the magnetic diffraction peak, located at 4.54 Å. The solid line was calculated from the best fit of Eq. (3) to the experimental data in the 523 K-T_N range.

The intensity of the satellite peak continuously decreases as temperature increases towards T_N, and is no longer observed for $T > T_N$. The temperature dependence of the satellite peak intensity in the 523 K-T_N temperature range is well described by the following equation [49,50]:

$$I(T) \propto (T_N - T)^{2\beta} = M^2(T). \tag{3}$$

From this analysis, we have found $\beta = 0.37 \pm 0.04$, which is in excellent agreement with the corresponding value ob-

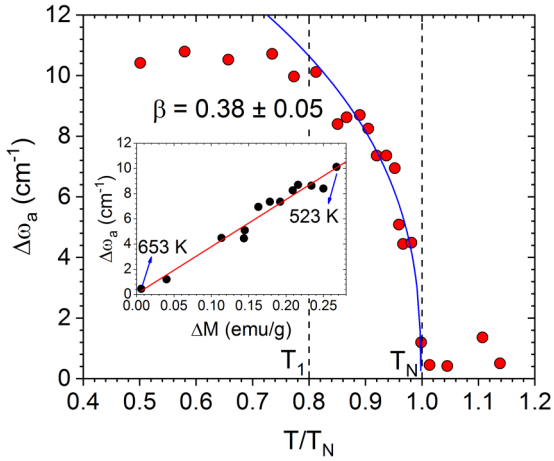

FIG. 7. Anomalous contribution to the wave number of the FeO_6 symmetric stretching mode ($\Delta\omega_a$) as a function of the reduced temperature T/T_N. The solid line was calculated fitting a similar equation to Eq. (2) in the 560–644 K range. Inset: $\Delta\omega_a$ as a function of the magnetization (ΔM), where the linear fit was performed between 523 and 653 K.

tained from the analysis of the $\Delta M(T)$ curve in the same temperature interval, revealing that the temperature dependence of the magnetic diffraction peak scales with the anomalous contribution to the magnetization. This result evidences a deep correlation between the structural modulation and the magnetic order parameter, highlighting that the stabilization of the magnetic phase in $Bi_{0.7}La_{0.3}FeO_3$ triggers the modulation of the crystalline structure, through lattice deformations, which we will address in the next section.

Now, we focus our attention on the peak at 4.54 Å, which has been assigned to a magnetic diffraction process [7,8]. To confirm this assumption, we have also analyzed the peak intensity as a function of the reduced temperature, shown in Fig. 6(c). As in the previous example, the intensity of the diffraction peak decreases as temperature increases, and it vanishes above T_N. Between 523 K and T_N, the temperature dependence of the diffraction peak intensity scales the square of magnetization, ascertained by the solid curved line determined from the best fit of Eq. (3) to the experimental results in that temperature range, with $\beta = 0.37 \pm 0.02$, which agrees very well with the value already referred to above, confirming the magnetic origin of the considered diffraction peak. Figure S4 in the Supplemental Material shows a quantitative comparison between these peak intensities and the $\Delta M^2(T)$ [39].

B. Spin-phonon coupling

The coupling between crystallographic and magnetic structures in $Bi_{0.7}La_{0.3}FeO_3$ is also mirrored by lattice excitations, as will be addressed in this section. Among the observed Raman-active phonons, the FeO_6 octahedra symmetric stretching mode exhibits the largest anomalous temperature behavior for temperatures below T_N. Figure 7 shows the reduced temperature dependence of the anomalous contribution to the wave number of the FeO_6 symmetric stretching mode ($\Delta\omega_a$), calculated from the difference of the extrapolation to $T < T_N$ of the best linear fit of the temperature dependence of the wave number of this mode above T_N and the experimental value, taken at the same temperature.

As temperature decreases from 737 K towards T_N, the wave number of the symmetric stretching mode follows the normal temperature dependence due to the anharmonic effects of thermal expansion, and just below T_N, a continuous increasing of the wave number upon further cooling is observed. The anomalous contribution $\Delta\omega_a(T)$ emerges at T_N and increases continuously for $T_1 < T < T_N$, reaching a constant value below $T_1 \sim 543$ K. The maximum value of $\Delta\omega_a(T)$ is 10 cm^{-1}. Similar anomalous temperature behavior has been reported for several Raman-active phonons in $BiFeO_3$ at the para-antiferromagnetic phase transition [51]. For instance, the wave number of the mode at 380 cm^{-1} (room-temperature value) exhibits the most expressive anomalous temperature behavior, with the maximum deviation of 20 cm^{-1} at 300 K [51]. Following the same analysis presented in Ref. [51], we have calculated the Grüneisen parameter associated with the wave-number hardening of the FeO_6 symmetric stretching mode ($\Delta\omega/\omega = \gamma\Delta V/V$, wherein V is the primitive cell volume), resulting in $\gamma = 33$; the reported value found in $BiFeO_3$ is $\gamma \sim 30$, which is similar to the one reported here. The rather large value for the Grüneisen parameter has been interpreted as a manifestation of mechanisms underlying the anharmonic effect other than the trivial temperature behavior [51]. To unravel this mechanism, we have performed a deeper analysis, taking into consideration that in magnetic orthorhombic perovskites, the octahedra symmetric stretching mode modulates the superexchange interactions between the B-site magnetic cations [52]. Following this idea, we have analyzed the temperature dependence of $\Delta\omega_a$ in the T_1-T_N range by fitting a similar equation to Eq. (2), as shown in Fig. 7. $\Delta\omega_a$ linearly scales with the anomalous contribution to the magnetization ΔM in the 523 K-T_N temperature range, as a similar exponent $\beta = 0.38 \pm 0.05$ is obtained. The linear scaling between $\Delta\omega_a$ and ΔM is better evidenced in the inset of Fig. 7, obtained in the T_1-T_N range. This result gives clear evidence for a structural change occurring at the magnetic phase transition, which involves octahedral distortions and an outstanding linear spin-phonon coupling in $Bi_{0.7}La_{0.3}FeO_3$. From this result, we can conclude that a magnetostructural coupling emerges in this material.

The large anomalous temperature dependence of the Raman modes found in both $BiFeO_3$ and $Bi_{0.7}La_{0.3}FeO_3$ contrast with the absent anomalous temperature dependence of the Raman modes of the rare-earth ferrites at the Néel temperature ($T_N \sim 623-740$ K, with increasing temperature for increasing rare-earth cation size) [53–55]. To explain such large frequency hardening, a mechanism other than the spin-spin correlation function was proposed for $BiFeO_3$, based on the coupling between electric polarization and magnetic ordering [51]. Such a mechanism can provide further support to corroborate the ferroelectric nature of $Bi_{0.7}La_{0.3}FeO_3$, already evidenced elsewhere [20,51].

According to Rusakov *et al.* [22], the driving force for the stabilization of the incommensurate modulated phase should be provided by a coupling between antipolar displacements of the Bi-O(1) chains and noticeable deformations of the FeO_6 octahedra. Our Raman results, concerning the nonvanishing increasing value of $\Delta\omega_a$ for $T < T_N$, not only provide clear

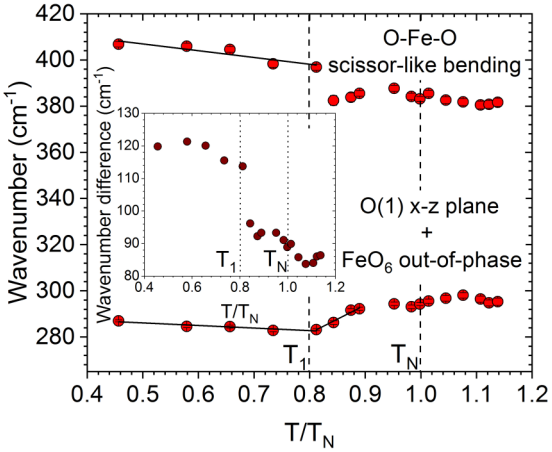

FIG. 8. Wave number of O(1) x-z plane + FeO_6 out-of-phase rotation band and O-Fe-O scissorlike bending mode as a function of the reduced temperature T/T_N. The solid lines are guides to the eye. Inset: wave-number difference between these two Raman bands as a function of T/T_N.

evidence for those octahedral deformations, but they also unravel that the stabilization of the IM phase is triggered by the magnetic ordering occurring at T_N through a noteworthy magnetostructural coupling mechanism.

C. Structural and magnetic critical events at T_1

The results previously presented in Fig. 6 provide evidence of anomalous changes in the temperature dependence of some quantities at around T_1 that correspond to the lower limit of the phase coexistence region, above which the *Pnma* phase starts gradually to emerge, and the modulation wave-vector magnitude starts to decrease monotonously. Together, this set of results points to the occurrence of significant structural changes at T_1 that also affect the magnetic properties via the magnetostructural coupling. In fact, the existence of structural distortions at T_1 is clearly apparent from the temperature dependence of the wave number of some Raman-active phonons, shown in Fig. 8.

In this work, we have focused our attention on two specific bands, the first assigned to the O(1) x-z plane and FeO_6 octahedra out-of-phase rotation modes, and the second to the O-Fe-O scissorlike bending mode. The first band probes the Bi-O(1) bond strength, while the second one probes the bending mode of the FeO_6 octahedra, giving complementary information regarding octahedral distortions.

From 294 K and up to T_1, both modes soften with a similar temperature rate of -0.02 cm^{-1}/K. The maximum variation of the wave number of both modes upon heating is about -8 cm^{-1}. Slightly above T_1, these modes exhibit an opposite shift of about 10 cm^{-1} (upward for the former and downward for the latter mode). This behavior yields an interesting temperature dependence of their wave-number difference, shown in the inset of Fig. 8, wherein a sudden downward jump of about 17 cm^{-1} is observed at around T_1, and a continuous decreasing is seen slightly above T_N. The existence of an anomalous temperature dependence of the wave number of these modes at T_1 points to lattice changes associated with the emergence of the *Pnma* phase.

D. Connection with simulations

The (T, x) phase diagram of $Bi_{1-x}La_xFeO_3$ has been an object of intense theoretical studies. However, no unique view of the structural phases and their stability range could be achieved until now, partially due to the plethora of different experimental results reporting different symmetries, namely in the intermediate x-range ($0.16 \leqslant x \leqslant 0.3$). Among them, tetragonal *P*4*mm* [56], monoclinic, and trigonal symmetries [57] have been proposed, but they were discarded due to the theoretical simulations recently reported. Moreover, many of the suggested room-temperature orthorhombic structures, such as $C222$, $C222_1$ [58], and *Imma* [22], may not correspond to stable phases of $Bi_{1-x}La_xFeO_3$, as they were not found to give any local energy minimum. The recently reported *Pbam* structure for the composition range $0.15 \leqslant x \leqslant 0.2$ at room-temperature conditions was found to be metastable [21,31,59]. The remaining *Pnma* and $Pna2_1$ phases have to be considered.

Focusing on the specific composition $Bi_{0.7}La_{0.3}FeO_3$, our work is perfectly consistent with and complements the simulation results published by González *et al.* [60]. According to those authors, for the composition range $0.3 \leqslant x \leqslant 0.65$, both the orthorhombic *Pnma* and $Pna2_1$ phases have similar energies and can coexist at room temperature. According to our findings, the $Pna2_1$ phase is the most stable one for $x = 0.3$ at room-temperature conditions. This is supported by the results obtained from the NPD experiment, and it is shown in Fig. S5 of the Supplemental Material: after heating the sample up to 733 K, the $Pna2_1$ NPD pattern profile is totally recovered at 343 K [39]. The predicted similar energies between both the orthorhombic *Pnma* and $Pna2_1$ phases explain very well the impressive large phase coexistence temperature interval of ~200 K that we report in this work. It is worth noting that in this discussion, the incommensurability of the room-temperature $Pn2_1a(00\gamma)000$ phase is not mentioned. However, once it has a magnetic origin, it should only emerge if magnetic terms in the simulation model are included, which is not actually the case.

V. CONCLUSIONS

In summary, we have investigated the high-temperature phase sequence of $Bi_{0.7}La_{0.3}FeO_3$ using high-resolution neutron powder diffraction and Raman spectroscopy. A detailed Pawley refinement analysis of the available NPD data, carried out from room temperature up to 733 K, reveals the existence of three different phase regions. First, a single IM region is observed up to T_1, described by the $Pn2_1a(00\gamma)000$ space group. Second, a coexistence phase region emerges between T_1 and an estimated temperature of 745 K, spanning over more than 200 K. At T_1 a *Pnma* phase starts to emerge, coexisting with the IM phase up to $T_N = 663$ K. Above this temperature the modulation vanishes, and the *Pnma* structure continues to coexist but with a $Pn2_1a$ phase instead. Finally, a single *Pnma* phase is stabilized above to ~745 K. These outcomes are fully supported by the analysis of the Raman data, wherein

the FeO_6 symmetric stretching, the O(1) *x-z* plane, the FeO_6 out-of-phase rotation, and the O-Fe-O scissorlike bending modes show anomalous temperature behavior, associated with structural and magnetic changes occurring at those temperatures. This feature yields clear evidence for the existence of a significant linear spin-phonon coupling in $Bi_{0.7}La_{0.3}FeO_3$.

Regarding the magnetic phase transition, we have obtained a critical exponent of $\beta = 0.384 \pm 0.003$ from the analysis of the magnetization data. A similar β value is obtained from the critical exponent analysis of the magnetic diffraction peak at 4.54 Å, the structural satellite peak at 4.90 Å, and the anomalous contribution $\Delta\omega_a$ to the wave number of the Raman-active FeO_6 symmetric stretching mode. Whereas the former result confirms the magnetic character of the peak, the two latter findings yield a definite outcome regarding the mechanisms associated with the magnetic phase transition. They show evidence for the emergence of specific magnetically mediated structural changes occurring at T_N, which involves the stabilization of a structural IM modulation, and specific anomalous octahedral distortions. Moreover, the linear scaling ascertained between $\Delta\omega_a$ and the magnetization reveals the existence of a significant magnetostructural coupling in this material. The phase coexistence region lower limit T_1, marking the emergence of the *Pnma* phase, can also be associated with the temperature wherein the modulation wave-vector magnitude starts to decrease. The anomalies observed at T_1 in the behavior of the O(1) *x-z* plane and the FeO_6 out-of-phase rotation band and O-Fe-O scissorlike bending mode point to subtle structural changes associated with the stabilization of the *Pnma* phase.

Finally, though it is not very clear from Ref. [22], our results point out that the upper temperature limit of the incommensurate modulated structural phase is a point on the paramagnetic-antiferromagnetic phase line. In fact, though the modulation is of a nonmagnetic nature, it is mediated by the magnetostructural mechanism ascertained below to T_N, which involves the oxygen octahedra.

ACKNOWLEDGMENTS

The authors would like to acknowledge Fundação para a Ciência e Tecnologia (FCT) through projects NORTE/01/0145/FEDER/028538, CERN/FIS-PAR/0005/2017, CERN/FIS-TEC/0003/2019, PTDC/FIS-MAC/29454/2017, and when appropriate cofinanced by ERDF under PT2020 Partnership Agreement: CQVR, projects UID/QUI/00616/2013 and UIDB/QUI/00616/2020; IFIMUP: Norte-070124-FEDER-000070; NECL: NORTE-01-0145-FEDER-022096, UID/NAN/50024/2019, CFisUC: UIDB/04564/2020 and UIDP/04564/2020; CICECO-Aveiro Institute of Materials: UIDB/50011/2020 and UIDP/50011/2020. M.M.G. and B.M. acknowledge the grants from the project PTDC/NAN-MAT/28538/2017. Experiments at the ISIS Pulsed Neutron and Muon Source were supported by a beamtime allocation from the Science and Technology Facilities Council, DOI: 10.5286/ISIS.E.RB1710261.

[1] J. F. Scott, Multiferroic memories, Nat. Mater. **6**, 256 (2007).
[2] S. Karimi, I. M. Reaney, Y. Han, J. Pokorny, and I. Sterianou, Crystal chemistry and domain structure of rare-earth doped $BiFeO_3$ ceramics, J. Mater. Sci. **44**, 5102 (2009).
[3] G. Catalan and J. F. Scott, Physics and applications of bismuth ferrite, Adv. Mater. **21**, 2463 (2009).
[4] C. Ederer and C. J. Fennie, Electric-field switchable magnetization via the Dzyaloshinskii-Moriya interaction: $FeTiO_3$ versus $BiFeO_3$, J. Phys.: Condens. Matter **20**, 434219 (2008).
[5] J.-G. Park, M. D. Le, J. Jeong, and S. Lee, Structure and spin dynamics of multiferroic $BiFeO_3$, J. Phys.: Condens. Matter **26**, 433202 (2014).
[6] D. Arnold, Composition-driven structural phase transitions in rare-earth-doped $Bifeo_3$ ceramics: A review, IEEE Trans. Ultrason. Ferroelectr. Freq. Contr. **62**, 62 (2015).
[7] I. Sosnowska, T. P. Neumaier, and E. Steichele, Spiral magnetic ordering in bismuth ferrite, J. Phys. C **15**, 4835 (1982).
[8] I. Sosnowska, M. Loewenhaupt, W. I. F. David, and R. M. Ibberson, Investigation of the unusual magnetic spiral arrangement in $BiFeO_3$, Physica B **180-181**, 117 (1992).
[9] J. Silva, A. Reyes, H. Esparza, H. Camacho, and L. Fuentes, $BiFeO_3$: A review on synthesis, doping and crystal structure, Integr. Ferroelectr. **126**, 47 (2011).
[10] Y. P. Wang, G. L. Yuan, X. Y. Chen, J.-M. Liu, and Z. G. Liu, Electrical and magnetic properties of single-phased and highly resistive ferroelectromagnet $BiFeO_3$ ceramic, J. Phys. D **39**, 2019 (2006).
[11] C.-H. Yang, D. Kan, I. Takeuchi, V. Nagarajan, and J. Seidel, Doping $BiFeO_3$: Approaches and enhanced functionality, Phys. Chem. Chem. Phys. **14**, 15953 (2012).
[12] T. T. Carvalho, B. Manjunath, J. Pérez de la Cruz, V. S. Amaral, J. R. A. Fernandes, A. Almeida, J. Agostinho Moreira, R. Vilarinho, and P. B. Tavares, Enhancement of resistivity and magnetization of $Bi_{1-x}La_xFe_{1-y}Mn_yO_3$ ceramics by composition optimization, J. Alloys Compd. **835**, 155404 (2020).
[13] S. R. Das, R. N. P. Choudhary, P. Bhattacharya, R. S. Katiyar, P. Dutta, A. Manivannan, and M. S. Seehra, Structural and multiferroic properties of La-modified $BiFeO_3$ ceramics, J. Appl. Phys. **101**, 034104 (2007).
[14] S. Zhang, L. Wang, Y. Chen, D. Wang, Y. Yao, and Y. Ma, Observation of room temperature saturated ferroelectric polarization in Dy substituted $BiFeO_3$ ceramics, J. Appl. Phys. **111**, 074105 (2012).
[15] M. Khodabakhsh, C. Sen, H. Khassaf, M. A. Gulgun, and I. B. Misirlioglu, Strong smearing and disappearance of phase transitions into polar phases due to inhomogeneous lattice strains induced by A-site doping in $Bi_{1-x}A_xFeO_3$ (A: La, Sm, Gd), J. Alloys Compd. **604**, 117 (2014).
[16] P. Uniyal and K. L. Yadav, Enhanced magnetoelectric properties in $Bi_{0.95}Ho_{50.05}FeO_3$ polycrystalline ceramics, J. Alloys Compd. **511**, 149 (2012).
[17] X. Zhang, Y. Sui, X. Wang, Y. Wang, and Z. Wang, Effect of Eu substitution on the crystal structure and multiferroic properties of $BiFeO_3$, J. Alloys Compd. **507**, 157 (2010).

[18] M. Polomska, W. Kaczmarek, and Z. Pajk, Electric and Magnetic Properties of $(Bi_{1-x}La_x)FeO_3$ solid solutions, Phys. Stat. Sol. **23**, 567 (1974).

[19] J. Bielecki, P. Svedlindh, D. T. Tibebu, S. Cai, S. G. Eriksson, L. Börjesson, and C. S. Knee, Structural and magnetic properties of isovalently substituted multiferroic $BiFeO_3$: Insights from Raman spectroscopy, Phys. Rev. B **86**, 184422 (2012).

[20] T. T. Carvalho, J. R. A. Fernandes, J. Perez De La Cruz, J. V. Vidal, N. A. Sobolev, F. Figueiras, S. Das, V. S. Amaral, A. Almeida, J. Agostinho Moreira, and P. B. Tavares, Room temperature structure and multiferroic properties in $Bi_{0.7}La_{0.3}FeO_3$ ceramics, J. Alloys Compd. **554**, 97 (2013).

[21] D. V. Karpinsky, I. O. Troyanchuk, O. S. Mantytskaja, G. M. Chobot, V. V. Sikolenko, V. Efimov, and M. Tovar, Magnetic and piezoelectric properties of the $Bi_{1-x}La_xFeO_3$ system near the transition from the polar to antipolar phase, Phys. Solid State **56**, 701 (2014).

[22] D. A. Rusakov, A. M. Abakumov, K. Yamaura, A. A. Belik, G. Van Tendeloo, and E. Takayama-Muromachi, Structural evolution of the $BiFeO_3$-$LaFeO_3$ system, Chem. Mater. **23**, 285 (2011).

[23] T. T. Carvalho and P. B. Tavares, Synthesis and thermodynamic stability of multiferroic $BiFeO_3$, Mater. Lett. **62**, 3984 (2008).

[24] A. Perejón, P. E. Sánchez-Jiménez, L. A. Pérez-Maqueda, J. M. Criado, J. Romero de Paz, R. Sáez-Puche, N. Masó, and A. R. West, Single phase, electrically insulating, multiferroic La-substituted $BiFeO_3$ prepared by mechanosynthesis, J. Mater. Chem. C **2**, 8398 (2014).

[25] V. Antonov, I. Georgieva, N. Trendafilova, D. Kovacheva, and K. Krezhov, First principles study of structure and properties of La- and Mn-modified $BiFeO_3$, Solid State Sci. **14**, 782 (2012).

[26] J.-H. Lee, M.-A. Oak, H. J. Choi, J. Y. Son, and H. M. Jang, Rhombohedral-orthorhombic morphotropic phase boundary in $BiFeO_3$-based multiferroics: First-principles prediction, J. Mater. Chem. **22**, 1667 (2012).

[27] P. Suresh and S. Srinath, Effect of La substitution on structure and magnetic properties of sol-gel prepared $BiFeO_3$, J. Appl. Phys. **113**, 17D920 (2013).

[28] Q. Zhang, X. Zhu, Y. Xu, H. Gao, Y. Xiao, D. Liang, J. Zhu, J. Zhu, and D. Xiao, Effect of La^{3+} substitution on the phase transitions, microstructure and electrical properties of $Bi_{1-x}La_xFeO_3$ ceramics, J. Alloys Compd. **546**, 57 (2013).

[29] I. O. Troyanchuk, M. V. Bushinsky, A. N. Chobot, O. S. Mantytskaya, and N. V. Tereshko, Weak ferromagnetism in $BiFeO_3$-based multiferroics, JETP Lett. **89**, 180 (2009).

[30] C. M. Kavanagh, R. J. Goff, A. Daoud-Aladine, P. Lightfoot, and F. D. Morrison, Magnetically driven dielectric and structural behavior in $Bi_{0.5}La_{0.5}FeO_3$, Chem. Mater. **24**, 4563 (2012).

[31] D. V. Karpinsky, I. O. Troyanchuk, M. Tovar, V. Sikolenko, V. Efimov, and A. L. Kholkin, Evolution of crystal structure and ferroic properties of La-doped $BiFeO_3$ ceramics near the rhombohedral-orthorhombic phase boundary, J. Alloys Compd. **555**, 101 (2013).

[32] A. A. Amirov, A. B. Batdalov, S. N. Kallaev, Z. M. Omarov, I. A. Verbenko, O. N. Razumovskaya, L. A. Reznichenko, and L. A. Shilkina, Specific features of the thermal, magnetic, and dielectric properties of multiferroics $BiFeO_3$ and $Bi_{0.95}La_{0.05}FeO_3$, Phys. Solid State **51**, 1189 (2009).

[33] I. O. Troyanchuk, D. V. Karpinsky, M. V. Bushinsky, O. S. Mantytskaya, N. V. Tereshko, and V. N. Shut, Phase transitions, magnetic and piezoelectric properties of rare-earth-substituted $BiFeO_3$ ceramics, J. Am. Ceram. Soc. **94**, 4502 (2011).

[34] B. H. Toby and R. B. Von Dreele, GSAS-II: The genesis of a modern open-source all purpose crystallography software package, J. Appl. Crystallogr. **46**, 544 (2013).

[35] J. Agostinho Moreira, A. Almeida, M. R. Chaves, M. L. Santos, P. P. Alferes, and I. Gregora, Raman spectroscopic study of the phase transitions and pseudospin phonon coupling in sodium ammonium sulphate dihydrate, Phys. Rev. B **76**, 174102 (2007).

[36] R. Przenioslo, A. Palewicz, M. Regulski, I. Sosnowska, R. M. Ibberson, and K. S. Knight, Does the modulated magnetic structure of $BiFeO_3$ change at low temperatures? J. Phys.: Condens. Matter **23**, 279501 (2011).

[37] A. S. Gibbs, D. C. Arnold, K. S. Knight, and P. Lightfoot, High-temperature phases of multiferroic $BiFe_{0.7}Mn_{0.3}O_3$, Phys. Rev. B **87**, 224109 (2013).

[38] A. D. Fortes and A. S. Gibbs, HRPD-X: A proposed upgrade to the ISIS high-resolution powder diffractometer, J. Neutron Res. **22**, 91 (2020).

[39] See Supplemental Material at http://link.aps.org/supplemental/10.1103/PhysRevB.104.174109 for parameters obtained from Pawley refinements of NPD patterns, Raman scattering spectra of the central peak component, temperature dependence of magnetization, intensities of satellite and magnetic peaks as a function of the square magnetization, and NPD patterns at different fixed temperatures in a heating run.

[40] D. Orobengoa, C. Capillas, M. I. Aroyo, and J. M. Perez-Mato, AMPLIMODES: Symmetry-mode analysis on the Bilbao crystallographic server, J. Appl. Crystallogr. **42**, 820 (2009).

[41] H. Toraya, A new method for quantitative phase analysis using x-ray powder diffraction: Direct derivation of weight fractions from observed integrated intensities and chemical compositions of individual phases, J. Appl. Crystallogr. **49**, 1508 (2016).

[42] M. Cazayous, Y. Gallais, A. Sacuto, R. De Sousa, D. Lebeugle, and D. Colson, Possible Observation of Cycloidal Electromagnons in $BiFeO_3$, Phys. Rev. Lett. **101**, 037601 (2008).

[43] Z. Xu, J. A. Schneeloch, J. Wen, M. Matsuda, D. Pajerowski, B. L. Winn, Y. Zhao, C. Stock, P. M. Gehring, T. Ushiyama, Y. Yanagisawa, Y. Tomioka, T. Ito, G. Gu, R. J. Birgeneau, and G. Xu, Spin-wave induced phonon resonance in multiferroic $BiFeO_3$, arXiv:1803.01041 [cond.mat.mtrl-sci].

[44] D. Treves, Studies on orthoferrites at the Weizmann Institute of Science, J. Appl. Phys. **36**, 1033 (1965).

[45] K. Park, H. Sim, J. C. Leiner, Y. Yoshida, J. Jeong, S. Yano, J. Gardner, P. Bourges, M. Klicpera, V. Sechovský, M. Boehm, and J.-G. Park, Low-energy spin dynamics of orthoferrites $AFeO_3$ (A = Y, La, Bi), J. Phys.: Condens. Matter **30**, 235802 (2018).

[46] M. Połomska, B. Hilczer, I. Szafraniak-Wiza, A. Pietraszko, and B. Andrzejewski, XRD, Raman and magnetic studies of $Bi_{1-x}La_xFeO_3$ solid solution obtained by mechanochemical synthesis, Phase Trans. **90**, 24 (2017).

[47] M. E. Fisher, The theory of equilibrium critical phenomena, Rep. Prog. Phys. **30**, 615 (1967).

[48] H. E. Stanley, *Introduction to Phase Transitions and Critical Phenomena* (Oxford University Press, New York, 1987).

[49] D. M. Pajerowski, C. R. Rotundu, J. W. Lynn, and R. J. Birgeneau, Magnetic neutron diffraction study of

$Ba(Fe_{1-x}Co_x)_2As_2$ critical exponents through the tricritical doping, Phys. Rev. B **87**, 134507 (2013).

[50] Y. J. Kim, S. Wakimoto, S. M. Shapiro, P. M. Gehring, and A. P. Ramirez, Neutron scattering study of AFM order in $CaCu_3Ti_4O_{12}$, Solid State Commun. **121**, 625 (2002).

[51] R. Haumont, J. Kreisel, P. Bouvier, and F. Hippert, Phonon anomalies and the ferroelectric phase transition in multiferroic $BiFeO_3$, Phys. Rev. B **73**, 132101 (2006).

[52] O. Delaire, M. B. Stone, J. Ma, A. Huq, D. Gout, C. Brown, K. F. Wang, and Z. F. Ren, Anharmonic phonons and magnons in $BiFeO_3$, Phys. Rev. B **85**, 064405 (2012).

[53] R. Vilarinho, *From Structural Distortions to Physical Properties in Orthorhombic Rare-Earth Perovskites* (Faculty of Sciences of University of Porto, Porto, 2019).

[54] A. Panchwanee, V. R. Reddy, A. Gupta, and V. G. Sathe, Study of spin-phonon coupling and magnetic field induced spin reorientation in polycrystalline multiferroic $GdFeO_3$, Mater. Chem. Phys. **196**, 205 (2017).

[55] Y. S. Ponosov and D. Y. Novoselov, Lattice and spin excitations of $YFeO_3$: A Raman and density functional theory study, Phys. Rev. B **102**, 054418 (2020).

[56] Z. X. Cheng, A. H. Li, X. L. Wang, S. X. Dou, K. Ozawa, H. Kimura, S. J. Zhang, and T. R. Shrout, Structure, ferroelectric properties, and magnetic properties of the La-doped bismuth ferrite, J. Appl. Phys. **103**, 07E507 (2008).

[57] P. Pandit, S. Satapathy, and P. K. Gupta, Effect of La substitution on conductivity and dielectric properties of $Bi_{1-x}La_xFeO_3$ ceramics: An impedance spectroscopy analysis, Physica B **406**, 2669 (2011).

[58] A. V. Zalesskii, A. A. Frolov, T. A. Khimich, and A. A. Bush, Composition-induced transition of spin-modulated structure into a uniform antiferromagnetic state in a $Bi_{1-x}La_xFeO_3$ system studied using 57Fe NMR, Phys. Solid State **45**, 141 (2003).

[59] D. V. Karpinsky, I. O. Troyanchuk, O. S. Mantytskaya, V. A. Khomchenko, and A. L. Kholkin, Structural stability and magnetic properties of $Bi_{1-x}La(Pr)_xFeO_3$ solid solutions, Solid State Commun. **151**, 1686 (2011).

[60] O. E. González-Vázquez, J. C. Wojdeł, O. Diéguez, and J. Íñiguez, First-principles investigation of the structural phases and enhanced response properties of the $BiFeO_3$_$LaFeO_3$ multiferroic solid solution, Phys. Rev. B **85**, 064119 (2012).